

Complex Dynamical Flow Phases and Pinning in Superconductors with Rectangular Pinning Arrays

C. Reichhardt and G.T. Zimányi

Department of Physics, University of California, Davis, California 95616.

Niels Grønbech-Jensen

Department of Applied Science, University of California, Davis, California 95616.

NERSC, Lawrence Berkeley National Laboratory, Berkeley, California 94720.

(October 30, 2018)

We examine vortex pinning and dynamics in thin-film superconductors interacting with square and rectangular pinning arrays for varied vortex densities including densities significantly larger than the pinning density. For both square and rectangular pinning arrays, the critical depinning force shows maxima at only certain integer matching fields where the vortices can form highly ordered arrays. For rectangular arrays the depinning force and commensurability effects are anisotropic with a much lower depinning threshold for vortex motion in the easy flow directions. We find evidence for a crossover in pinning behavior in rectangular pinning arrays as the field is increased. We also show analytically, and confirm with simulations, that for $B = 2B_\phi$ the strongest pinning can be achieved for rectangular pinning arrangements rather than square for one direction of driving force. Under an applied driving force we find a remarkable variety of distinct complex flow phases in both square and rectangular arrays. These flow phases include stable sinusoidal and intricate pinched patterns where vortices from different channels do not mix. As a function of the driving force certain flow states become unstable and transitions between different phases are observed which coincide with changes in the net vortex velocities. In the rectangular arrays the types of flow depend on the direction of drive. We also show that two general types of plastic flow occur: stable flows, where vortices always flow along the same paths, and unstable or chaotic flows.

I. INTRODUCTION

Vortex pinning in systems where defects are arranged in periodic arrays are an ideal system in which to study optimal pinning arrangements and commensurability effects since the properties of the pinning sites, such as the size, periodicity of the array, and array geometry, can be highly controlled. These arrays can be fabricated using nano-lithography techniques in which periodic arrangements of micro-holes [1–12] or magnetic dots [13–19] of various geometries can be constructed. A more recent technique is the use of Bitter decoration where the magnetic particles used for the initial decoration can act as well ordered arrays of pinning [15]. In these systems commensurability effects can be observed in the form of peaks in the critical current at fields where the number of vortices equals an integer or a fraction of the number of pinning sites. At these commensurate fields the vortices can form a highly ordered lattice where vortex-vortex interactions which reduce the effective pinning are minimized, while at incommensurate fields the vortex lattice can be disordered and vortex-vortex interactions make the pinning less effective. Direct imaging of vortex structures with square pinning arrays have been conducted with Lorentz microscopy [9] and scanning Hall-probes [10] which have confirmed that the vortices form highly ordered crystals at the integer and some fractional matching fields. These images along with simulations [23] have

also shown that at the different matching fields different types of ordered vortex crystals can be stabilized. In the samples imaged by Harada *et al.*, [9] it was found that beyond the first matching field all the pinning sites are occupied with a single vortex and that the additional vortices sit in the interstitial regions. The particular vortex lattice symmetry found at the second matching field was square; at the third matching field there was an ordered lattice with alternating pairs of interstitial vortices; while at the fourth matching field the overall lattice was triangular. The same types of ordered vortex lattice crystals were also seen in simulations with square pinning arrays and additional types of stable vortex crystals were observed for triangular pinning arrays [23]. Recent scanning Hall-probe experiments [10] have found various ordered rational fractional fillings less than the first matching field and have also shown that for fields greater than the first matching field, vortices can have both multiple occupancy per pinning site as well as vortices that are located in the interstitial regions.

Most experimental studies of vortex matter interacting with periodic pinning have considered square and triangular pinning lattices. Some recent studies, however, have been performed with Kagome pinning arrays, which produced pronounced matching effects at non-integer matching fields [14]. Periodic arrangements with rectangular geometries of magnetic dots [18,19] and holes [17,21,22] have also been studied recently. In these systems there can be two periodicities associated with the

two sides of the rectangular cell, a and b . In experiments with magnetic dots [18,19] a field dependent crossover in the commensurability effects was observed. Sharp low field matching effects occurring at every integer matching field were found to cross over to much broader matching effects occurring at fields where the vortex density matches with the periodicity of the short side of the rectangular pinning array. In these systems one would expect an anisotropic response, with a lower pinning or easy flow direction through the wide end of the rectangular cell since the flow of interstitial vortices will be less impeded by the vortices pinned by the dots. Additionally one would still expect an anisotropic response due to increased vortex-vortex interactions along the short end of the cell at the incommensurate fields which will lower the pinning force for fields less than the first matching field, as well as for fields greater than the first matching field when multiple occupancy per pinning site occurs. Recent magneto-optical imaging experiments in samples with rectangular pinning arrays have found evidence for anisotropic vortex flow [21]. Anisotropic pinning has also been observed in related systems where the individual pinning sites have an anisotropic geometry [20].

In square pinning arrays recent simulations have shown that a remarkable number of distinct dynamical phases are possible when the number of vortices is larger than the number of pinning sites. These phases include one-dimensional flow of interstitial vortices, random plastic flow, soliton-like flow along the pinning sites, and coherently moving elastic flow phases [24]. Other simulations of vortices in systems with periodic pinning arrays have also observed transitions from different types of plastic flow to elastic flow [26,27]

Experiments and simulations have also examined the pinning and dynamics of vortices through thin channels [28–30], where the vortices moving through the channels experience a periodic potential created by the ordered lattice of vortices that are immobile outside of the channels. Peaks in the critical current are observed where the vortices in the channel can form a commensurate ordering. Additionally simulations [30] have shown that a wide variety of dynamical phases occur such as soliton like flow, and a periodic winding motion of vortices.

Experimentally, evidence for the flow of interstitial vortices in samples with periodic pinning arrays where individual pinning sites are small has been observed in transport measurements and current-voltage curves [8]. Shapiro steps for the 1D flow of interstitial vortices between pinning sites with an AC and DC applied driving has been observed in experiments [11] and simulations [25]. Direct imaging of vortices using Lorentz microscopy has demonstrated the 1D flow of interstitial vortices between pinning sites as well as pulse-like motion of vortices along pinning sites and between the pinning sites. The pulse or soliton flow of vortices along the symmetry directions of the pinning arrays has also been observed with

magneto-optical imaging [6].

In systems with random pinning under an applied driving force the vortex lattice can exhibit different types of transport behavior such as plastic flow, where the vortex lattice is highly disordered or liquid like and a portion of the vortices can remain immobile while other portions can tear past. There can also be elastic flow where the moving vortices keep the same neighbors and the overall lattice structure can have a crystalline or smectic order. As a function of applied driving force transitions or crossovers can occur between different flow phases. Evidence for such transitions has been observed in transport measurements [31], voltage noise [32], neutron scattering [33], Bitter-decoration [34,35], and STM [36] and simulations [37–40]. These moving phases have also been studied theoretically [41].

In this work we present the results of simulations for vortices in 2D superconductors interacting with square and rectangular pinning arrays. In particular we examine the pinning characteristics and the dynamical states. In previous simulations [23] only square and triangular pinning arrays were examined and the dynamical flow states were only examined in detail for filling fractions less than 2.25. In addition previous simulations calculated the magnetization curves but did not calculate the depinning force directly from current-voltage curves. Here, we examine anisotropic pinning by considering rectangular pinning arrays for $a/b = 2, 1.6$, and 1 under applied driving. We have also calculated analytically the critical currents in the a and b direction at the second matching fields as a function of a/b and find that the critical current is optimal not for $a/b = 1$ but for a rectangular geometry when driven in certain directions. For square pinning arrays we find much more pronounced matching effects at integer and fractional matching fields for low applied fields; however, for higher fields the matching effects are reduced and certain peaks are absent, in agreement with recent experiments [12]. For rectangular arrays with $a/b = 2$ we find that the shape and strength of the commensurability effects at the matching fields depends on whether the driving is in the a or b direction. The depinning force is much higher along the long direction. We also find evidence for a crossover in the commensurability effects at high fields. Images of the vortices in the rectangular pinning array show that highly ordered vortex crystals are stabilized at the matching fields where a peak in the depinning force is observed, while more disordered crystals are formed at the matching fields where peaks are not observed.

Under an applied driving force we show that a remarkable variety of complex dynamical phases emerge in square and rectangular arrays. These phases depend strongly on the geometry of the pinning lattice. Despite the complexity of these dynamic phases two general classes of flow can be identified. The first is elastic flow of a mobile sub-lattice of interstitial vortices between

pinned vortices with the vortex motion in stable well defined patterns. The other type of flow is a chaotic or mixing flow where the interstitial vortex motion is disorderly. The moving channels show a mixing effect, in that the vortices from one channel move to other channels. The stable, non-mixing flow phases occur only for certain integer matching fields and rational machining fields. As a function of applied driving force dynamical transitions between different types of flow states are possible which coincide with features in the driving force versus velocity curves or voltage-current curves which can be detected experimentally.

II. SIMULATION

We simulate a thin superconductor where the vortices can be considered as 2D objects interacting with a logarithmic potential, $u_v = -\ln(r)$, where energy is normalized to $A_v = \Phi_0^2/8\pi\Lambda$, Φ_0 being the flux quantum and Λ the effective 2D penetration depth for a thin film superconductor. The normalized overdamped equation of motion for a vortex i is

$$\mathbf{f}_i = \frac{d\mathbf{r}_i}{dt} = \mathbf{f}_i^{vv} + \mathbf{f}_i^{vp} + \mathbf{f}_d = \mathbf{v}_i. \quad (1)$$

The normalized force on vortex i from the other vortices is $\mathbf{f}_i^{vv} = -\sum_{j \neq i}^{N_v} \nabla_i U_v(r_{ij})$, where $U_v(r_{ij})$ is the effective, re-summed, vortex-vortex potential between two vortices in a computational cell with periodic boundary conditions [42]. Pinning is modeled as attractive parabolic wells with

$$\mathbf{f}_i^{vp} = -(f_p/r_p)\Theta(r_p - |\mathbf{r}_i - \mathbf{r}_k^{(p)}|)\hat{\mathbf{r}}_{ik}^{(p)}. \quad (2)$$

Θ is the Heaviside step function, $\mathbf{r}_k^{(p)}$ is the location of pinning site k , f_p is the maximum pinning force, $\hat{\mathbf{r}}_{ik}^{(p)} = (\mathbf{r}_i - \mathbf{r}_k^{(p)})/|\mathbf{r}_i - \mathbf{r}_k^{(p)}|$, and r_p is the radius of the pinning sites. The pinning sites are placed in a rectangular array (nL_x, mL_y) , where n and m are integers. The characteristic length, by which all lengths are normalized, is chosen to be $r_0 = \frac{10}{3}r_p$. In a typical experiment $L_x = 400-900$ nm and the pinning radius is 125 nm. The characteristic time in the normalized equation of motion is $\tau = \eta r_p^2/A_v$, where η is the Bardeen-Stephen friction. The equation of motion is numerically integrated by an Euler method using a normalized time step of $dt = 0.02$.

The initial vortex positions are obtained from annealing by a high temperature, where we add a Langevin noise term \mathbf{f}_i^T to equation (1) such that $\langle \mathbf{f}_i^T \rangle = 0$ and $\langle \mathbf{f}_i^T(t) \cdot \mathbf{f}_j^T(t') \rangle = 4T\delta_{ij}\delta(t-t')$, where T is the temperature normalized to A_v/k_B , k_B being the Boltzmann constant. We choose an initial temperature high enough such that the vortices are in a molten state and cool to $T = 0$ in 20 increments where we allow 20000 time steps between each increment. After annealing, the driving force

is slowly increased from $f_d = 0$ and the vortex positions and velocities are monitored using $V_x = \sum_i^{N_v} \hat{\mathbf{x}} \cdot \mathbf{v}_i$ and $V_y = \sum_i^{N_v} \hat{\mathbf{y}} \cdot \mathbf{v}_i$. In this work we consider simulations where the driving is only in the x -direction or y -direction. The depinning force is defined as the force at which the vortex velocities reach $0.03f_d$.

III. CRITICAL FORCE AT $B = 2B_\phi$

We first consider analytically the depinning threshold in the case of the vortex lattice driven in the x or y directions at $B = 2B_\phi$ for arbitrary L_x and L_y . At this filling fraction the vortex lattice consists of the vortices at the pinning sites along with well ordered interstitial vortices located between the vortices at the pinning sites. We make the assumption that the unpinned vortices form a perfect rectangular lattice, so that they effectively do not interact due to symmetry. With this assumption we need to consider only the depinning of a single interstitial vortex moving in the periodic potential created by the vortices at the pinning sites. The vortex will move one-dimensionally along the direction of the drive and experience the periodic potential created by the vortices at the pinning sites.

$$\frac{dx_i}{dt} - f_i^{vv}(x_i, y_i) = f_d. \quad (3)$$

The vortex-vortex interaction term $f_i^{vv}(x, y)$ can be calculated using the re-summation method for logarithmically interacting particles in 2D [42]; the resulting equation of motion for an interstitial vortex (i) moving at $y_i = \frac{1}{2}L_y$ along the x -direction is:

$$\frac{dx_i}{dt} - \frac{\pi}{L_x} \sum_{k=-\infty}^{\infty} \frac{\sin(2\pi \frac{x_i}{L_x})}{\cosh\left(2\pi \frac{L_y}{L_x} \left(k + \frac{1}{2}\right)\right) - \cos(2\pi \frac{x_i}{L_x})} = f_d. \quad (4)$$

The maximum depinning force will occur when the summation term is maximum. In the limit of $L_y \ll L_x$, this happens for $x_i = \frac{3}{4}L_x$, and the resulting critical force is,

$$f_x^c = \frac{2\pi}{L_x} \operatorname{sech}\left(\pi \frac{L_y}{L_x}\right). \quad (5)$$

This expression is accurate for $L_x \lesssim 1.5L_y$ (the error is about 0.2% for $L_x = L_y$ and about 5% for $L_x = 2L_y$). By symmetry, we trivially write the corresponding critical force in the y -direction, for $L_x \ll L_y$, to be given by,

$$f_y^c = \frac{2\pi}{L_y} \operatorname{sech}\left(\pi \frac{L_x}{L_y}\right), \quad (6)$$

which is then accurate for $L_y \lesssim 1.5L_x$.

In figure 1 we plot the critical force in the x -direction and y -direction from equations (5) and (6) where L_y is kept at a fixed value of 2.0 and L_x is varied from 4.0 to 1.25. For all increasing L_y/L_x the critical force in the x -direction is reduced. This can be understood by considering that the pinning of the interstitial vortices is caused by the interactions with the vortices at the pinning sites. With no driving an interstitial vortex will sit in the center of the rectangle where the forces from the vortices at the pinning sites cancel. For decreasing L_y/L_x , the interstitial vortices will have to move through a narrower channel between vortices at the pinning sites in the y -direction so the interaction between the interstitial vortices and the pinned vortices will increase. For driving along the y direction, for L_y/L_x decreasing from 1, the critical force is reduced. This can be understood by considering that as L_x is reduced the interstitial vortex interactions with the pinned vortices in front of the interstitial vortices and those behind will increasingly cancel. As L_y/L_x is increased from 1 the opposite occurs with the interaction of the vortices that push on the interstitial vortices becoming reduced.

Experimentally the behavior of the critical currents as predicted from equations (5) and (6) can also be used to determine whether interstitial vortices are present at $B/B_\phi = 2$ as opposed to multiple vortices at individual pinning sites. In the case of multiple vortices at the pinning sites the depinning force would be independent of the ratio of L_y/L_x since the depinning force will not be determined by the interactions between the vortices due to the symmetry of the overall multi-vortex lattice, but will instead be determined from the strength of the pinning site only. We also show in Fig. 1 the simulation results for the square ($L_y/L_x = 1.0$) and rectangular cases ($L_y/L_x = 2.0$ and $L_y/L_x = 0.5$) for driving in the x and y directions showing excellent agreement with the predicted values.

Another experimental signature of interstitial vortices is the strong difference in the critical force between the x and y directions at $L_y = 2L_x$. The critical force in the y direction is already more than 50 times higher than the critical force in the x -direction. Even experiments with a relatively small anisotropy ratio such as $L_y/L_x = 1.25$ should see $f_c^x/f_c^y \approx 3$.

These results also show that the maximum pinning can be achieved not with square arrays but with rectangular arrays. This enhancement is only for one of the directions of driving. Figure 1 shows that the depinning force for $L_y = 2L_x$ in the y -direction is about 2.5 times higher than for the square case. In practice the ratio of L_y/L_x has a finite range in which it can be varied due to the finite size of the pinning sites.

We note that we could calculate analytically the depinning force only at $B = 2B_\phi$, or for any other B values where the interstitial-interstitial vortex interactions effectively cancel. However, away from the B values leading

to high symmetry interstitial configurations, the depinning forces should still be anisotropic. The depinning force for an interstitial vortex near a single interstitial vacancy will be reduced from its value at $B = 2B_\phi$ by a quantity $\propto 1/L_x$ if driven in the x direction and $\propto 1/L_y$ if driven in the y direction since the vortex-vortex force goes like $\propto 1/r_{ij}$. Similar arguments for an anisotropic depinning force can be made for additional interstitial vortices added to the $B = 2B_\phi$ vortex configurations.

IV. DEPENDENCE OF DEPINNING FORCE ON B/B_ϕ IN A SQUARE ARRAY

In Fig. 2 we show the dependence of the critical depinning force as a function of B/B_ϕ for a system with a square pinning array. Here sharp peaks in f_p^c can be seen at $B/B_\phi = 1, 2, 3, 4$, and 5. Smaller peaks are seen for $B/B_\phi = 6$ and 8. At $B/B_\phi = 7$ there is no evidence for a peak. Another interesting feature is that for $6 < B/B_\phi < 8$ the critical force remains at an intermediate value which is higher than the lowest critical current values for $B < 5B_\phi$. This is a similar trend to that observed by Metlushko *et al.* [12] who claim that interstitial vortices are present for $B/B_\phi > 1$ due to the small size of the pinning sites. The peaks observed in Fig. 2 are much stronger than those observed in magnetization measurements in simulations with flux-gradient driven vortices with short range interactions [23]. In that work commensuration enhancements were not seen at $B/B_\phi = 3, 6$, or 7. The vortex configurations observed at the matching fields are the same as those for Ref [26]. Another feature in Fig. 2 is that the height of the peaks for $B < 5B_\phi$ shows variations with the largest peak at $B = 4B_\phi$ when the vortices form a triangular lattice as seen in simulations and experiments. Some experiments with square and magnetic dots have observed strong matching effects at *every* matching field [13] suggesting the presence of multi-vortex states in these systems. The inset of Fig. 2 shows the depinning curve for a system with the same parameters as Fig. 2, but with the pinning sites in a random arrangement. Here the depinning force decreases with increasing field and there are no peaks at the matching fields.

In Fig. 2 commensurability peaks at the fractional fields $1/2, 3/2$, and $5/2$ can also be observed. Peaks in the critical current at fractional B/B_ϕ have been seen in experiments with particularly pronounced peaks at $1/2$ and $3/2$ while weaker peaks were seen at $1/4, 1/5$, and $1/16$ [3]. The vortex configurations and dynamics at fractional matching fields are studied in detail elsewhere. We do not observe any particular fractional matching except at $B/B_\phi = 8.5$ where a clear peak in the critical current is observed. Such a commensuration peak has not been seen in previous simulations or experiments. In section

V (c) we show that a stable non-mixing flow state occurs at this field.

V. DYNAMICAL FLOW STATES FOR SQUARE PINNING ARRAYS

A. 1D Flow States at $B/B_\phi = 2, 4$ and 9

Figure 3(a) shows the flow states just above depinning for $B/B_\phi = 2$ where the motion consists of the straight 1D flow of interstitial vortices between the pinned vortices. This type of flow was also seen in simulations at the same field for vortices with bulk interactions. In Fig. 3(b) for $B/B_\phi = 4$ a similar 1D straight vortex flow is observed. Here the vortices at the pinning sites also remain pinned and there are additional interstitial vortices located between the pinning sites in the x direction that also remain pinned. The mobile interstitial vortices can move in a straight unhindered 1D path while the immobile interstitial vortices cannot move in 1D paths without entering a pinning site or coming close to the vortices located in the pinning sites. In Fig. 3(c) at $B/B_\phi = 9$ the same type of 1D interstitial flow as in Fig. 3(a) and Fig. 3(b) is observed but in this case there are two mobile rows of vortices between the pinning sites and two immobile interstitial vortices between vortices at the pinning sites. In Fig. 3(a,b,c) the vortex motion can be seen to be elastic with respect to the mobile vortices in which the moving vortices keep their same moving neighbors. Further, the vortices always flow in the same paths. At fields with a fraction of 0.05 higher or lower than the matching fields in Figs. 3(a,b,c) the initial vortex motion occurs at the location of the extra vortex or vacancy in the ordered interstitial lattice. The depinning occurs at a lower driving force than that at which the commensurate vortex configuration depins. The flow of these extra interstitials or vacancies will again be in a 1D path along the direction of drive; however, the motion is not continuous but occurs in a soliton or pulse fashion with the extra interstitial or vacancy exchanging places with pinned vortices as it propagates. A similar soliton like motion of vortices along the pinning sites has also been observed previously in simulations [23] and experiments [6].

B. Sinusoidal Flow States At $B/B_\phi = 5, 8$, and 8.5

In Fig. 4(a) we show the flow states at $B/B_\phi = 5$ which shows sinusoidal flow states of the interstitial vortices. Here the vortex motion is not strictly 1D in the direction of drive but shows a periodic motion in the transverse direction as well. In addition the vortices flow in the same paths and vortices from one channel do not mix with vortices in the other channels. In Fig. 4(b) a similar sinusoidal flow as seen at $B/B_\phi = 5$ is observed with

an additional square sub-lattice of pinned interstitial vortices at the center of the pinning plaquette similar to the vortex configuration at $B/B_\phi = 2$. For higher drives the immobile interstitial vortices depin and the vortex lattice enters a new flow phase. In Fig. 4(c) for $B/B_\phi = 8.5$, where a small peak in the critical current is seen, an interesting flow state is observed where there is a pinned interstitial lattice for every other interstitial vortex in the middle of the pinning array plaquette. Additionally there are two immobile vortices between pinning sites in the x -direction. The vortex flow is a combination of 1D flow and sinusoidal flow with the sinusoidal flow occurring at every other plaquette containing a pinned interstitial vortex.

C. Bistable Flow States in the Vicinity of $B/B_\phi = 3$

Fig. 5(a,b) shows typical vortex flow patterns observed for fields $2.75 < B/B_\phi < 3.5$. Here the interstitial vortices move in periodic meandering paths around the pinned vortices. Interestingly the direction of the vortex flow is *not* in the direction of the driving force but at 45 degrees in either transverse direction. Since either direction is equivalent the flow jumps between the two states as seen in the measured transverse V_y velocities. In Fig. 6, V_y shows a small amplitude periodic component caused by the winding nature of the vortex flow, along with low frequency large amplitude jumps of V_y from positive to negative indicating that the net vortex motion direction is changing. For different system sizes the characteristic of the flow paths remains the same. Experimentally this flow state can be observed with transverse noise measurements. For stronger drives there is a transition to a more disordered flow in the direction of the driving force.

D. Disordered Vortex Flow States and Noise

In Fig. 7(a,b,c) we show the vortex flow states at various incommensurate fields showing varying degrees of disordered or mixing flow states. In Fig. 7(b) the vortex trajectories for $B/B_\phi = 4.95$ are plotted showing that the general features of the stable channel flow from $B/B_\phi = 5$ are still present. There are, however, now some vortices that can be seen to jump between adjacent channels. In Fig. 7(a) for $B/B_\phi = 4.5$ the vortex trajectories are more disordered and no discernible preferred channels are visible. This same type of flow is seen for $B/B_\phi = 5.5$. There are regions near the pinning sites where repulsion from the vortices located in the pinning sites keeps other vortices from approaching closer than a certain distance. In Fig. 7(c) we show the vortex trajectories for $B/B_\phi = 7$ showing that the disordered flow is again similar to what was seen at $B/B_\phi = 4.5$. We

note that this is the matching field at which a peak was absent in the depinning force. In general we observe that the non-mixing flows occur only near certain integer or fractional matching fields where the initial pinned vortex lattice has an ordered state. The flows then become increasingly disordered as the fields move away from these matching configurations.

To further compare the experimentally measurable noise signals of the ordered and disordered vortex states we plot in Fig. 8 the time series and the corresponding Fourier transforms (FT's) of the average vortex velocity V_x for a fixed applied driving force. Each data set is analyzed for 30,000 MD steps. In the figures we only show a portion of the time series for clarity. For $B/B_\phi = 4$ (Fig. 8(a,b)), where the flow was seen to occur in 1D channels as seen in Fig. 3(b), only a single periodic component and higher harmonics can be seen. For $B/B_\phi = 4.5$ (Fig. 8(c,d)) where the flow was disordered as seen in Fig. 7(a), a more random noise signal is observed and the FT shows a broad spectra. At $B/B_\phi = 5$ (Fig. 8(e,f)) where an ordered flow state was observed as seen in Fig. 4(a), a clear single frequency signal is again observed. In Fig. 9 we show the time series and FT for $B/B_\phi = 3$ where more complicated vortex trajectories were observed as seen in Fig. 5(a,b). Here the signal shows several different periodicities. In general we find periodic signals where orderly or partially ordered flows are observed, and broad noise spectra where incommensurate or disorderly flows occur.

E. Longitudinal and Transverse Noise

In Fig. 10(a,b) we show the time series for both the sum of the velocities in the x -direction and y -direction simultaneously for (a) $B/B_\phi = 4$ and (b) $B/B_\phi = 5$. For $B/B_\phi = 4$ longitudinal velocities show the periodic signal as shown earlier while the transverse velocities are zero as the vortices are moving strictly in the x -direction in 1D channels as seen in Fig. 3(b). For $B/B_\phi = 5$ both the longitudinal and transverse velocities show a pronounced periodic signal as the vortex trajectories show a sinusoidal flow as seen in Fig. 4(a). These results suggest that the features of the flow, such as whether it is winding in the transverse direction or strictly 1D, can be probed experimentally with transverse noise measurements. The periodic time signals at the matching fields can also be probed with an applied AC drive superimposed on a DC drive. Shapiro steps can be observed, as recently determined in experiments and simulations at $B/B_\phi = 2$. Where the vortex flows are highly ordered one would then expect Shapiro steps [25], while at the disordered flow states the phase-locked steps would be absent or strongly reduced.

VI. DEPENDENCE OF DEPINNING FORCE ON FIELD FOR RECTANGULAR PINNING ARRAYS

A. Rectangular Pinning Array with $L_x/L_y = 2$

In Fig. 11(a,b) we show the dependence of the critical depinning force on B/B_ϕ for systems with similar parameters as studied for the square array with $L_x = 2L_y$ for driving in the x -direction and y -direction. Here f_x^c is much higher than f_y^c for all $B > B_\phi$. For $B/B_\phi < 6$ commensurability peaks are observed for driving in both the x and y directions; however, the peaks in the x -direction do not show the sharpness of the peaks seen for the y -direction. The peaks for both driving directions are much broader for $B/B_\phi > 5$. There are no clear peaks at $B/B_\phi = 7$ or 9; however, there is some evidence for a drop-off in the depinning force right after these fields.

B. Vortex Configurations for $L_x/L_y = 2$

In Fig. 12(a-i) we show the vortex configurations for the various matching fields. The vortex configurations at $B/B_\phi = 1$ and 2 (Figs. 12(a,b)) are rectangular in order. For $B/B_\phi = 3$ (Fig. 12(c)) the vortex crystal has a diagonal ordering. At $B/B_\phi = 4$ (Fig. 12(d)) a square vortex lattice is stabilized. At $B/B_\phi = 5$ (Fig. 12(e)) the vortex lattice does not form a simple rectangular lattice but an ordering is still present as indicated by the unit cell. We note that at $B/B_\phi = 5$ a peak or anomaly in the depinning force is not observed. For $B/B_\phi = 6$ and 8, ordered distorted hexagonal vortex lattices are stabilized. At $B/B_\phi = 7$ and 9 the vortex lattice is disordered which again corresponds to there being no peaks in the critical depinning force. These results indicate that at the matching fields where an ordered lattice with a simple rectangular or hexagonal ordering can occur, an enhancement in the critical current can be observed.

VII. DYNAMICAL FLOW STATES FOR RECTANGULAR PINNING ARRAYS

In Fig. 13(a-f) we show the flow states at depinning in the rectangular arrays for $B/B_\phi = 2, 3, 4, 5, 6,$ and 9, respectively, for driving along the long side or x -direction. 1D flows that are similar to those seen in the square arrays occur for $B/B_\phi = 2$ and 6 (Fig. 13(a) and Fig. 13(e)). Disordered flow phases occur for $B/B_\phi = 3, 4$ and 9 (Fig. 13(b), Fig. 13(c) and Fig. 13(f)) where only minimal anomalies were seen in the depinning force. A disordered phase is also observed for $B/B_\phi = 7$ (not shown) where there was again no anomaly in the depinning force. An ordered flow phase is observed for $B/B_\phi = 8$ which is described in the next section where a peak in the depinning is observed. At $B/B_\phi = 5$

(Fig. 13(d)), where a static ordered lattice was stabilized but an anomaly in the depinning force was not observed, we find an interesting periodic winding flow of interstitial vortices. Also pairs of immobile interstitial vortices are located between every other pair of pinning sites.

A. Pinched Sinusoidal Flow For $B/B_\phi > 5$ for Driving Along the Short Edge

A new type of stable flow phase that appears for the rectangular arrays for $B/B_\phi > 4$ at higher drives is a *pinched sinusoidal* flow phase such as seen in Fig. 14(d) for $B = 8$. We follow the development of this phase in Fig. 14 for $B/B_\phi = 8$ where the initial depinning occurs through the almost 1D flow of interstitial vortices where two interstitial vortices remain pinned between the pinning sites as seen in Fig. 14(a) where $f_d = 0.1$. There is additional slower periodic wandering of the moving vortices in the y -direction that broadens the channel. This periodic transverse wandering of the channels can also be seen to push the immobile interstitial vortices in the transverse direction. The trajectories from the longitudinally moving vortices are pinched where the moving vortices are directly adjacent to the pinning sites. In Fig. 14(b) with $f_d = 0.2$ we show that for increased driving forces there is a transition to a disordered state as the immobile interstitial vortices begin to depin. For $f_d = 0.3$ (Fig. 14(c)) the flow starts to reorganize to the pinched sinusoidal flow which becomes fully developed for $f_d = 0.325$ as seen in Fig. 14(d).

In the pinched sinusoidal flow the vortices show a stable channel flow similar to the sinusoidal flows seen in the square arrays; however there is a pinched feature as the vortices flow adjacent to the pinning sites. As the vortices move through the pinched area only one vortex goes through the intersections at a time with a vortex from the upper and lower part of the branches alternating. For the other matching fields for $B/B_\phi > 4$ the same type of flow patterns are observed. The same flow patterns are observed at fields not too far from commensuration with the mobile rows carrying a varying number of vortices.

B. Additional Dynamical Flow Phases for $B/B_\phi < 4$

In Fig. 15(a) we show an interesting type of dynamically induced rotational motion ordered flow phase that occurs at and near $B/B_\phi = 2.5$ for driving along the long side of the pinning lattice. The depinning is due to the 1D flow of a portion of the interstitial vortices which move between every other pinning row. Another portion of interstitial vortices cannot pass through the pinned vortices and show a remarkable paired collective rotational motion. The rotations occurs as a pair of interstitial vortices

rotate in opposite directions as the 1D moving interstitial vortices pass. Additionally every other rotating pair is out of phase with the adjacent rotating pairs. The rotational motion occurs due to the fact that the rotating interstitial vortices are located in a shallow potential well created by the vortices located at the pinning sites. As the ordered 1D moving vortices move past they push the interstitial vortices that are not moving longitudinally. Although these pairs do not show a net motion in the x -direction they are still taking part in the dissipation and slow down the 1D moving vortices. For higher drives the rotating interstitials can be dislodged from their orbits and the flow becomes more disordered.

In Fig. 15(b) we show the ordered flow phase that occurs for $B/B_\phi = 4.5$ where the initial depinning occurs through the sinusoidal flow of a portion of the interstitial vortices. Unlike the previous sinusoidal flows observed in this case the channels weave across the pinning sites rather than strictly between two rows of pinning sites. For higher drives the other immobile vortices depin and the flow enters a disordered phase.

C. Flow Phases For Driving Along Long Edge

In Fig. 16(a-f) we show the flow states just above depinning for driving along the short side of the rectangular pinning array for $B/B_\phi = 2, 3, 4, 7, 8,$ and 9 , respectively. The motion at $B = 2B_\phi$ (Fig. 16(a)) is 1D where a single channel of interstitials is moving while for $B/B_\phi = 8$ (Fig. 16(e)) three rows of vortices are flowing and an immobile interstitial vortex is located between the pinning sites. An almost 1D flow is seen at $B/B_\phi = 7$ (Fig. 16(d)) in which 3 rows of interstitial vortices are moving. We note that for $B/B_\phi = 7$ a peak or matching anomaly was not present. The vortex configurations for $B/B_\phi = 7$ shows that along the immobile row of vortices there are 16 vortices with 8 located in the pinning sites while the mobile rows each contain 13 vortices so that the moving vortices are not commensurate with the periodicity of the potential created by the immobile vortices. For the $B/B_\phi = 8$ matching field where a peak was seen, the vortex configurations again show 16 vortices along the immobile row but the moving rows each contain 16 vortices which can be commensurate with the immobile vortices. The flow paths for $B/B_\phi = 3$ (Fig. 16(b)) and $B/B_\phi = 4$ (Fig. 16(c)) each show two rows of moving interstitial vortices in a sinusoidal flow with the flow at $B/B_\phi = 4$ showing a larger amplitude. For $B/B_\phi = 9$ (Fig. 16(f)) where there was an absence of the peak in the depinning force the flow is mostly disordered with some remnant of the flow phase seen at $B/B_\phi = 8$.

In Fig. 17(a,b) we show the flow phase at $B/B_\phi = 5,$ and $6,$ respectively, for driving along the short edge. The flow at $B/B_\phi = 7$ shows a remarkable *braiding* flow where the moving interstitial vortices flow in a crossing

pattern. A moving vortex that starts in the region almost underneath the pinning sites will move at an angle until it reaches the opposite side of the channel two pinning sites up while other vortices cross in the opposite direction. At $B/B_\phi = 6$ a similar flow to that seen at $B/B_\phi = 5$ is observed; however, the motion is not perfectly ordered.

VIII. CONCLUSION

We have analyzed numerically the vortex pinning and dynamics in square and rectangular pinning arrays for thin film superconductors. We predict an anisotropic critical current for the rectangular pinning arrays and calculate analytically the ratio of the critical depinning forces for different aspect ratios at $B/B_\phi = 2$. These results show that as the critical current is enhanced in one direction it is reduced in the other direction. The maximum critical current can be achieved for driving in certain directions of the rectangular pinning array. Numerical simulations also find that the anisotropy in the critical depinning force occurs for $B/B_\phi < 4$ and is less pronounced for higher fields. In the case of the square pinning arrays we observe pronounced commensurability effects at most integer matching fields and a missing matching peak at $B/B_\phi = 7$ in good agreement with recent experiments.

In the rectangular pinning arrays with an aspect ratio of 2:1 we observe an anisotropic depinning threshold in which the easy flow direction shows an overall lower depinning force but sharper and more pronounced commensuration effects while in the other direction the overall depinning force at both the commensurate and non-commensurate fields is higher, but the matching effects are considerably reduced. We observe integer matching effects in both driving directions up to $B/B_\phi = 5$, after which only every other matching field shows an enhanced critical current. The vortex configurations show that at the matching fields where enhanced critical currents are observed an ordered vortex arrangement is formed while at the matching fields where there is no enhancement the vortex arrangement is disordered.

For both the square and rectangular arrays we find that a remarkable variety of intricate dynamical flow phases can be realized and in general two classes of flow phases can be observed: stable channel flow, where vortices flow in the same paths in identifiable channels and vortices from one channel do not mix with vortices in another channel; and a disordered or mixing flow, where vortices from different channels mix or no identifiable channels occur. The particular flow states we observe include a 1D flow of interstitial vortices. For the square arrays at $B/B_\phi = 5, 6, 8$ and 8.5 a sinusoidal flow occurs where a portion of the interstitial vortices are moving in winding paths while another portion of interstitial vortices remain pinned along with the vortices at the pinning sites. For

increasing drives the immobile interstitial vortices can depin and the vortices can enter a more disordered flow phase. Near $B/B_\phi = 3$ a remarkable bistable flow phase is observed where the vortex flow is not in the direction of drive, but is alternating from the $+45$ degree direction to the -45 degree direction. This motion can also be seen in the transverse vortex velocities. Away from commensurability these ordered flow phases become increasingly disordered. We also show that these phases can be probed experimentally with noise spectra. In ordered phases the noise spectra shows distinctive narrow-band features, while the disordered flows show a broad spectra. In addition we show that with transverse noise measurements the 1D and sinusoidal flows can be distinguished where the sinusoidal flows will show a narrow band transverse signal.

In the rectangular arrays several of the phases observed in the square arrays are also observed. A new ordered flow phase that occurs for driving in the short direction for a wide range of fields for high driving is a braided channel flow. At the matching fields the braided flow is uniform with each channel carrying the same number of vortices while at incommensurate fields the channels can carry different numbers of vortices. The signature of the onset of this braided flow can be seen in the current-voltage characteristics.

Acknowledgments

We thank C.J. Olson for critical reading of this manuscript, and I.K. Schuller, J. Martin, L.E. DeLong, L. Van Look, V. Metlushko, V.V. Moshchalkov, A. Hoffman, F. Nori, and R.T. Scalettar for useful discussions. This work was supported by the Director, Office of Advanced Scientific Computing Research, Division of Mathematical, Information and Computational Sciences of the U.S. Department of Energy under contract number DE-AC03-76SF00098 as well as CLC and CULAR (Los Alamos National Laboratory).

-
- [1] A.T. Fiory, A.F. Hebard, and S. Somekh, *Appl. Phys. Lett.* **32**, 73 (1978).
 - [2] V. Metlushko *et al.*, *Solid State Commun.* **91**, 331 (1994).
 - [3] M. Baert *et al.*, *Phys. Rev. Lett.* **74**, 3269 (1995); V.V. Moshchalkov *et al.*, *Phys. Rev. B* **54**, 7385 (1996); V.V. Moshchalkov *et al.*, *Phys. Rev. B*, 3615 (1998); V. Metlushko *et al.*, *Phys. Rev. B* **59**, 603 (1999).
 - [4] M. Baert *et al.*, *Europhys. Lett.* **29**, 157 (1995).
 - [5] J.Y. Lin *et al.*, *Phys. Rev. B* **54**, R12714 (1996); A. Castellanos *et al.*, *Appl. Phys. Lett.* **71**, 962 (1997).
 - [6] R. Surdeanu, R.J. Wijngaarden, R. Wordenweber, and R. Griessen, to be published.

- [7] A. Bezryadin, Yu. B. Ovchinnikov, and B. Pannetier, Phys. Rev. B **53**, 8553 (1996).
- [8] E. Rosseel *et al.*, Phys. Rev. B **53**, R2983 (1996).
- [9] K. Harada *et al.*, Science **271**, 1393 (1996).
- [10] S. Field *et al.*, cond-mat/0003415; A.N. Grigorenko *et al.*, to be published.
- [11] L. Van Look *et al.*, Phys. Rev. B **60**, R6998 (1999).
- [12] V. Metlushko *et al.*, Phys. Rev. B **60**, R12 585 (1999).
- [13] J.I. Martín *et al.*, Phys. Rev. Lett. **79**, 1929 (1997); Y. Jaccard *et al.*, Phys. Rev. B **58**, 8232 (1998); A. Hoffman, P. Prieto and I.K. Schuller, Phys. Rev. B **61**, 6958 (2000).
- [14] D.J. Morgan and J.B. Ketterson, Phys. Rev. Lett. **80**, 3614 (1998).
- [15] Y. Fasano *et al.*, Phys. Rev. B **60**, R15047 (1999).
- [16] A. Terentiev, D.B. Watkins, L.E. De Long, D.J. Morgan and J.B. Ketterson, Physica C **324**, 1 (1999); A. Terentiev *et al.*, Phys. Rev. B **61**, R9249 (2000).
- [17] V.V. Metlushko *et al.*, Europhysics Letters **41**, 333 (1998).
- [18] J.I. Martín *et al.*, Phys. Rev. Lett. **83**, 1022 (1999).
- [19] J.I. Martín *et al.*, Phys. Rev. B **62**, 9110 (2000).
- [20] L. Van Look *et al.*, to be published.
- [21] S. Kolesnik *et al.*, to be published.
- [22] V.V. Metlushko *et al.*, to be published.
- [23] C. Reichhardt, C.J. Olson, and F. Nori, Phys. Rev. B **57**, 7937 (1998).
- [24] C. Reichhardt, C.J. Olson, and F. Nori, Phys. Rev. Lett. **78**, 2648 (1997).
- [25] C. Reichhardt, R.T. Scalettar, G.T. Zimányi, and N. Grønbech-Jensen, Phys. Rev. B **R11 914** (2000).
- [26] V.I. Marconi and D. Domínguez, Phys. Rev. Lett. **82**, 4922 (1999); cond-mat/0008125.
- [27] K.D. Fisher, D. Stroud, and L. Janin, Phys. Rev. B **60**, 15371 (1999).
- [28] A. Pruyjboom *et al.*, Phys. Rev. Lett. **60**, 1430 (1988); M.H. Theunissen *et al.*, *ibid.*, **77**, 159 (1996).
- [29] S. Anders *et al.*, Physica C **332**, 35 (2000); and to be published.
- [30] R. Besseling, R. Niggebrugge, and P.H. Kes, Phys. Rev. Lett. **82**, 3144 (1999).
- [31] S. Bhattacharya and M.J. Higgins, Phys. Rev. Lett. **70**, 2617 (1993); M.J. Higgins and S. Bhattacharya, Physica C **257**, 232 (1996); M.C. Hellerqvist *et al.*, Phys. Rev. Lett. **76**, 4022 (1996); W. Henderson *et al.*, Phys. Rev. Lett. **77**, 2077 (1996).
- [32] A.C. Marley, M.J. Higgins and S. Bhattacharya, Phys. Rev. Lett. **74**, 3029 (1995).
- [33] U. Yaron *et al.*, Nature **376**, 753 (1995).
- [34] A. Duarte *et al.*, Phys. Rev. B **53**, 11336 (1996); F. Pardo *et al.*, Phys. Rev. Lett. **78**, 2644 (1997).
- [35] F. Pardo *et al.*, Nature **396**, 348 (1998).
- [36] A.M. Troyanovski, J. Aarts, and P.H. Kes, Nature **399**, 665 (1999).
- [37] A.E. Koshelev and V.M. Vinokur, Phys. Rev. Lett. **73**, 3580 (1994).
- [38] K. Moon, R.T. Scalettar, and G.T. Zimányi, Phys. Rev. Lett. **77**, 2278 (1996); S. Ryu *et al.*, Phys. Rev. Lett. **77**, 5114 (1996).
- [39] H.J. Jensen, A. Brass and A.J. Berlinsky, Phys. Rev. Lett. **60**, 1676 (1988); A.Ch-Shi and A.J. Berlinsky, Phys. Rev. Lett. **67**, 1926 (1991); N. Grønbech-Jensen, A.R. Bishop, and D. Domínguez, Phys. Rev. Lett. **76**, 2985 (1996); M.C. Faleski, M.C. Marchetti, and A.A. Middleton, Phys. Rev. B **54** 12427 (1996); S. Spencer and H.J. Jensen, Phys. Rev. B **55**, 8473 (1997); D. Domínguez, Phys. Rev. Lett. **82**, 181 (1999); A.B. Kolton, D. Domínguez, N. Grønbech-Jensen, Phys. Rev. Lett. **83**, 3061 (1999).
- [40] C.J. Olson, C. Reichhardt, and F. Nori, Phys. Rev. Lett. **81**, 3757 (1998).
- [41] T. Giamarchi and P. Le Doussal, Phys. Rev. Lett. **76**, 3580 (1996); **78**, 752 (1997); P. Le Doussal and T. Giamarchi, Phys. Rev. B **57**, 11 356 (1998); L. Balents, M.C. Marchetti, and L. Radzihovsky, Phys. Rev. Lett. **78**, 751 (1997); Phys. Rev. B **57**, 7705 (1998); S. Scheidl and V.M. Vinokur, Phys. Rev. E **57**, 2574 (1998).
- [42] N. Grønbech-Jensen, Int. J. Mod. Phys. C **7**, 873 (1996); N. Grønbech-Jensen, Comp. Phys. Comm. **119**, 115 (1999).

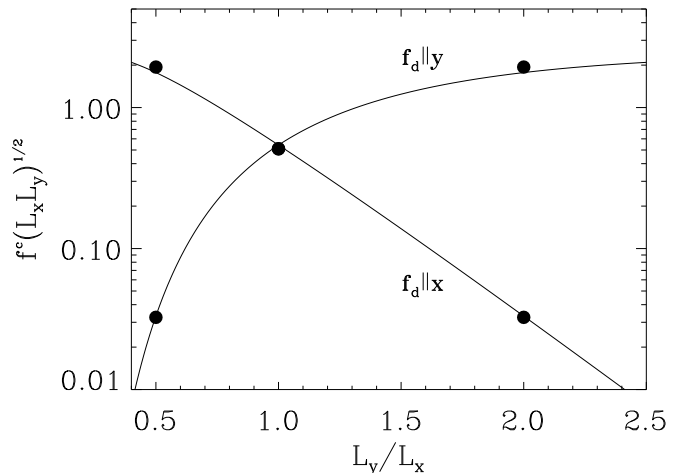


FIG. 1. Critical depinning force for driving in the x -direction and y -direction vs the aspect ratio of the rectangular pinning array for $B = 2B_\phi$ as predicted by Eq. (5) and Eq. (6) for a constant $L_y = 2.0$ with L_x varied from 4.0 to 1.25. The filled circles are the results from simulations.

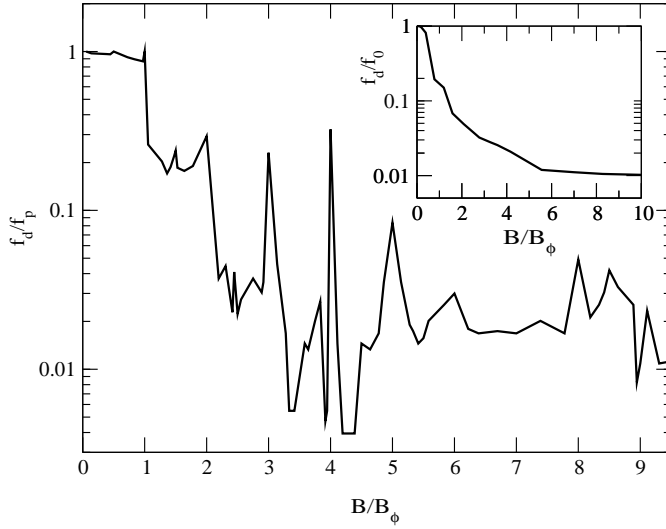


FIG. 2. Critical depinning force vs the field B/B_ϕ in a system with a square pinning array for $nL_x = nL_y = 12.0$. Peaks in the depinning force can be seen at most of the matching fields with a clear missing peak at $B/B_\phi = 7$. In addition some clear peaks can be seen at the fractional matching fields $B/B_\phi = 1/2, 3/2$ and $5/2$. The inset shows the depinning force vs B/B_ϕ for a system with the same parameters but with the pinning sites in a random arrangement showing the absence of matching effects.

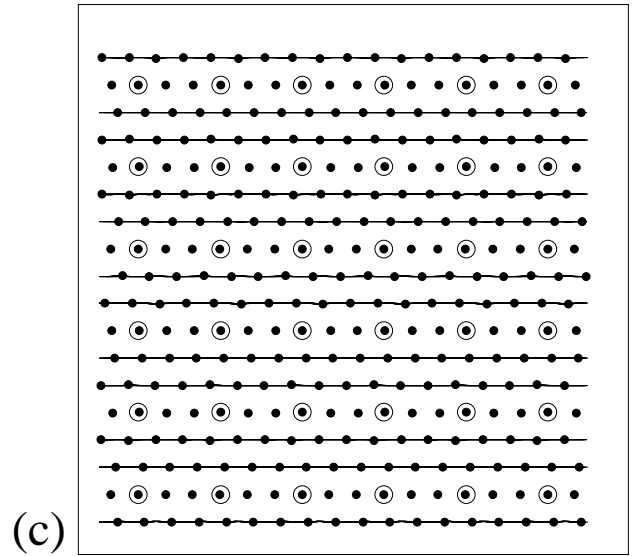
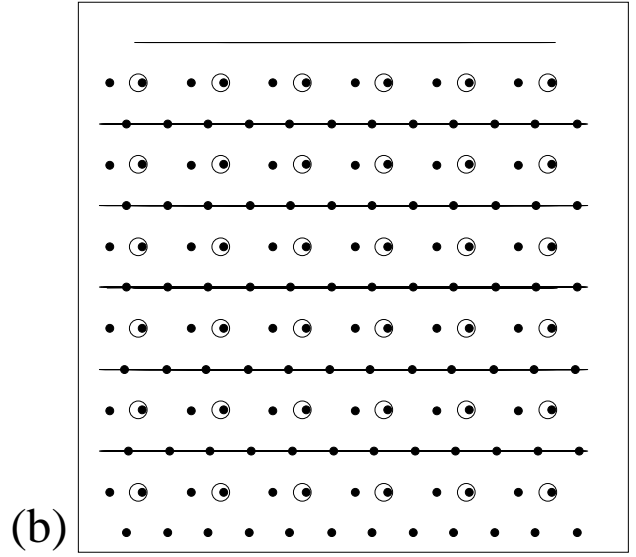
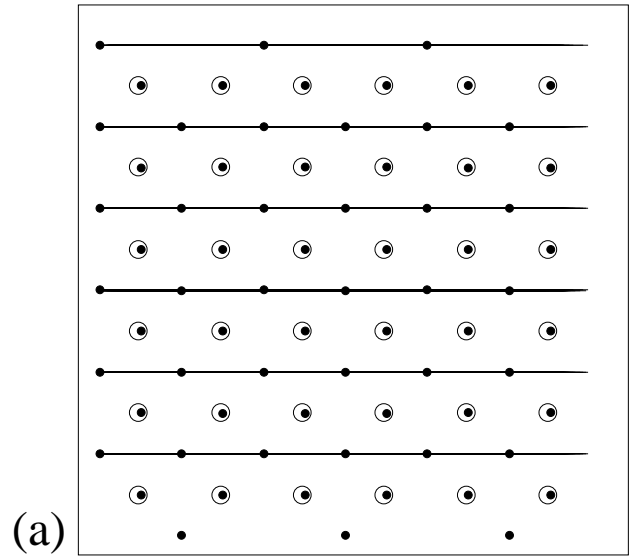


FIG. 3. Vortex trajectories for the system in Fig. 2 just above depinning for (a) $B/B_\phi = 2$, showing the 1D flow of single rows of interstitial vortices. (b) $B/B_\phi = 4$, showing the 1D flow of 2 rows of vortices between pinning sites. Between each pair of pinning sites is a single immobile interstitial vortex. (c) $B/B_\phi = 9$, showing the 1D flow where 3 rows of vortices flow between the pinning sites while a pair of immobile interstitial vortices are located between the pinning sites.

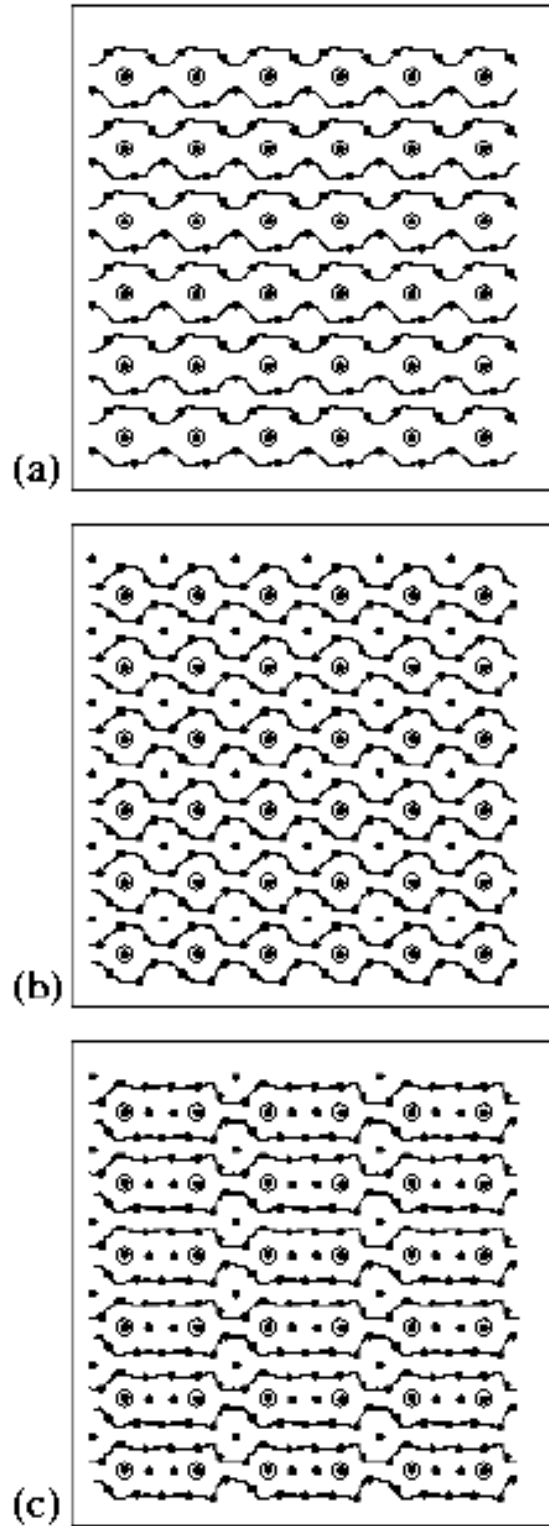


FIG. 4. Vortex trajectories just above depinning for (a) $B/B_\phi = 5$ showing that the flow occurs with two periodic winding rows of mobile vortices moving between each pinning row. (b) $B/B_\phi = 8$ showing a more sinusoidal like flow where again two rows of vortices move between the pinning rows. In addition, in the center of each pinning plaquette is an immobile interstitial vortex. (c) $B/B_\phi = 8.5$ shows a pinched flow. An immobile interstitial vortex is located in the center of every other plaquette and a pair of immobile interstitial vortices are located between every other pair of pinning sites.

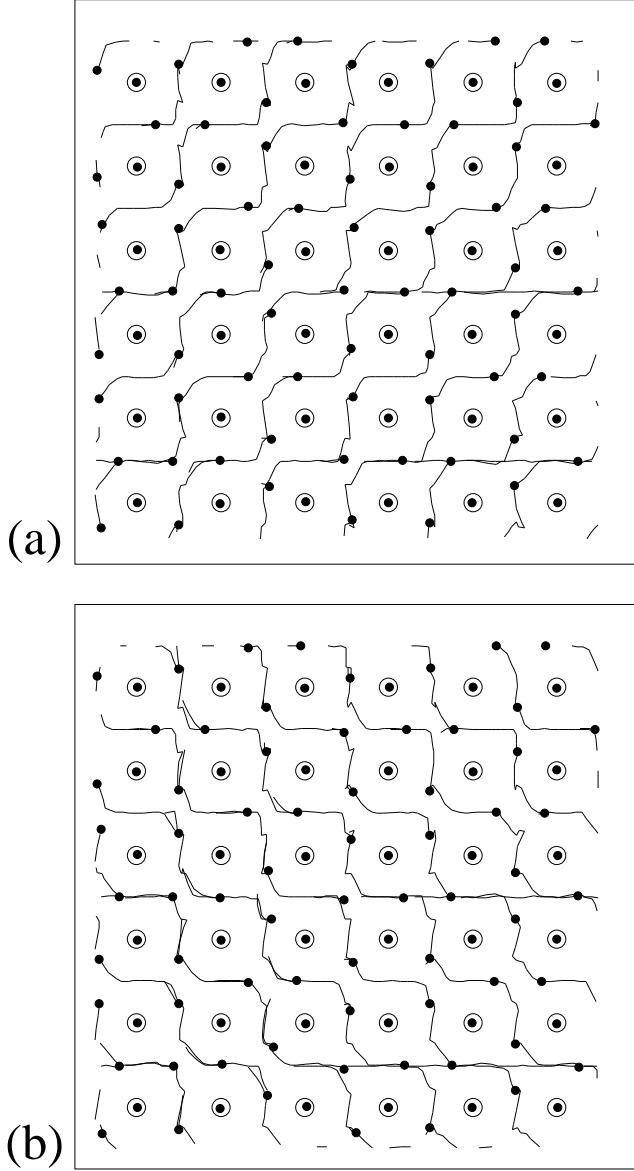


FIG. 5. (a) Vortex trajectories for $B/B_\phi = 3$ showing the periodic winding vortex motion at $+45^\circ$. (b) The vortex trajectories for the same system and time interval as in (a) after the vortex motion switches to the -45° .

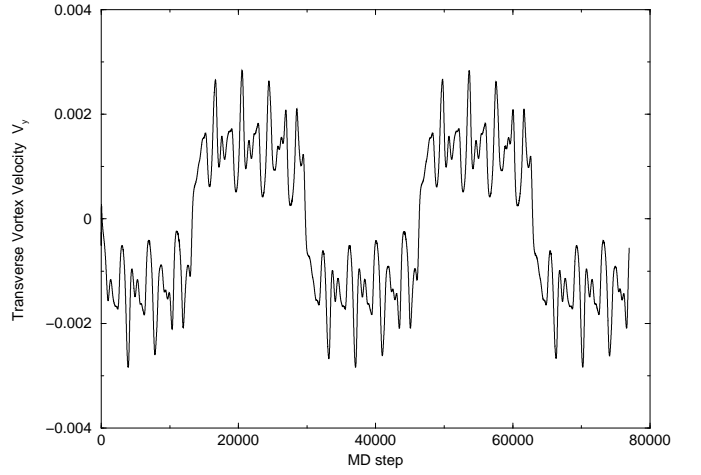


FIG. 6. Transverse, or y -direction, vortex velocities for the system in Fig. 5 where the driving is in the x -direction. The vortex motion locks into the $\pm 45^\circ$ direction for 150000 MD steps before switching to the other direction. The additional smaller scale periodic component is due to the winding nature of the vortex flow in the channels as seen in Fig. 5.

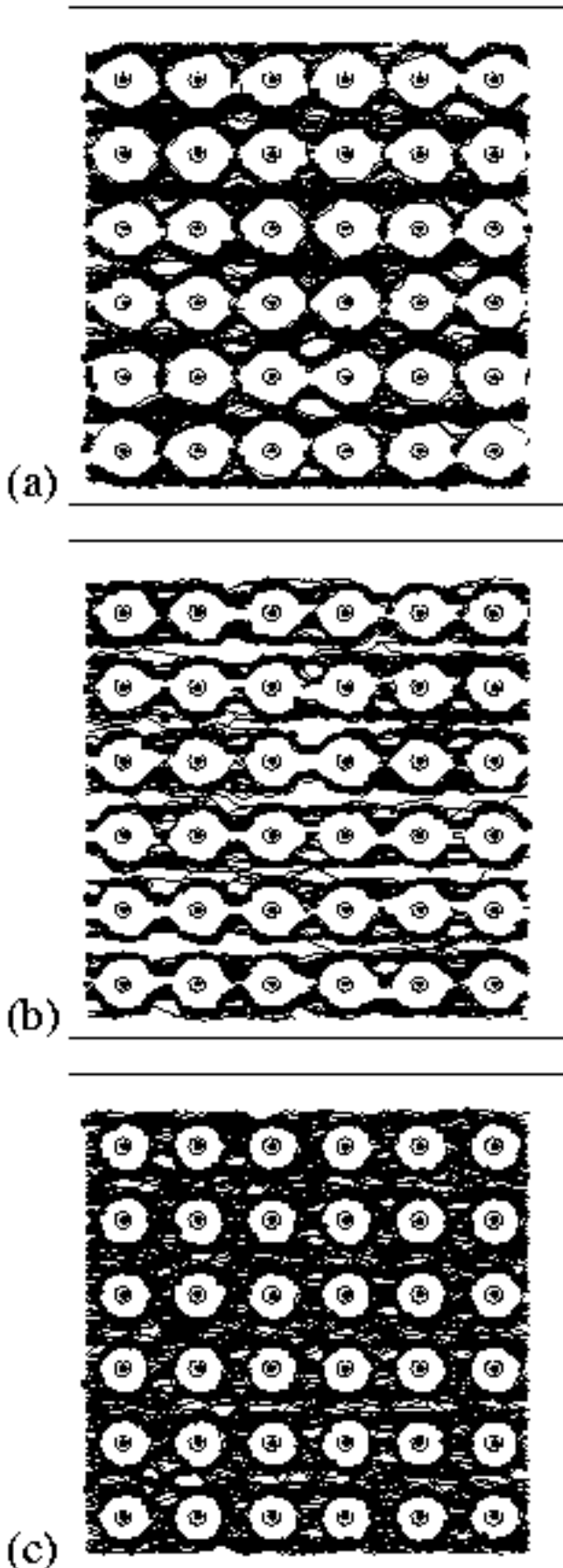


FIG. 7. Vortex trajectories for (a) $B/B_\phi = 4.5$ showing a disordered flow where the trajectories change over time. Vortices do not move through the regions near the occupied pinning sites due to the vortex-vortex repulsion. (b) $B/B_\phi = 4.95$, showing that flow is more ordered with the same features of the periodic winding channels observed at $B/B_\phi = 5$. If the trajectories are drawn for a longer time the plots become increasingly smeared and the plot will become indistinguishable from that seen in (a). (c) The vortex trajectories for the same time interval as in (a) and (b) for $B/B_\phi = 7$ showing a disordered flow pattern.

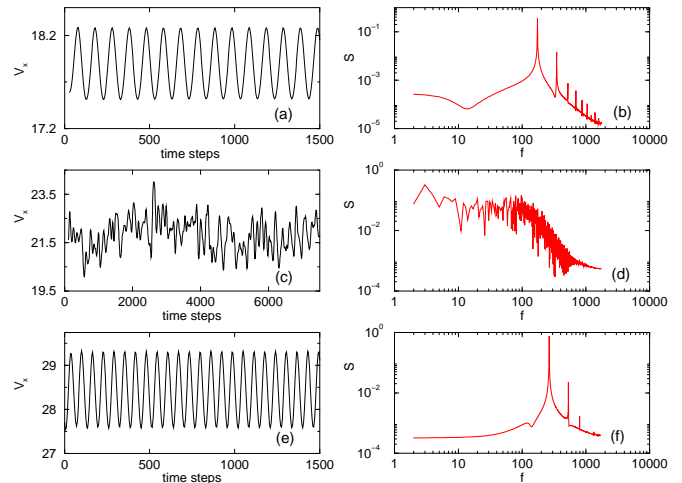


FIG. 8. Time series of the sum of longitudinal vortex velocities and Fourier transforms for the vortex flow. (a,b) $B/B_\phi = 4$ where a periodic signal occurs due to the 1D flow of vortices (Fig. 3(b)) through the periodic potential created by the pinned vortices. (c,d) $B/B_\phi = 4.5$ where a broad spectra occurs due to the disordered flow as seen in Fig. 7(a). (e,f) $B/B_\phi = 5$ where again a periodic signal occurs as the vortices move in periodic winding channels as seen in Fig 4(a). The FT's were taken on data sets of 30000 MD steps.

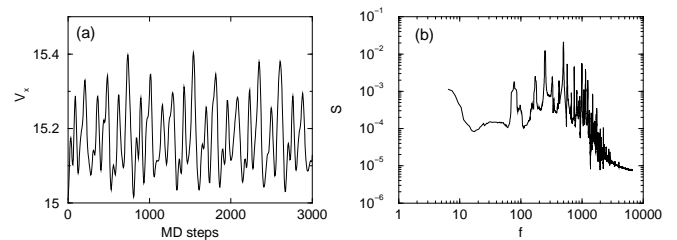


FIG. 9. Time series of the sum of the longitudinal vortex velocities and Fourier transform for the vortex flow at $B/B_\phi = 3$, where the flow occurs in winding channels. Here several different periodicities can be distinguished.

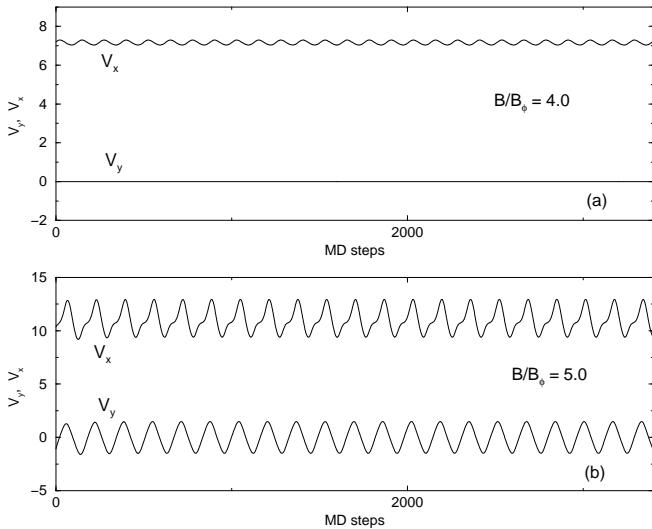


FIG. 10. The time series for the sum of the longitudinal velocities V_x and transverse velocities V_y for (a) $B/B_\phi = 4$ and (b) $B/B_\phi = 5$ for a fixed drive of $f_d/f_p = 0.4$. In (a) where the vortex motion occurs by the 1D flow of interstitial vortices as seen in Fig. 3(b) the longitudinal velocities show a periodic component while the transverse velocity is zero. For (b) where the vortex motion was sinusoidal both the x and y components of the velocities show a periodic signal.

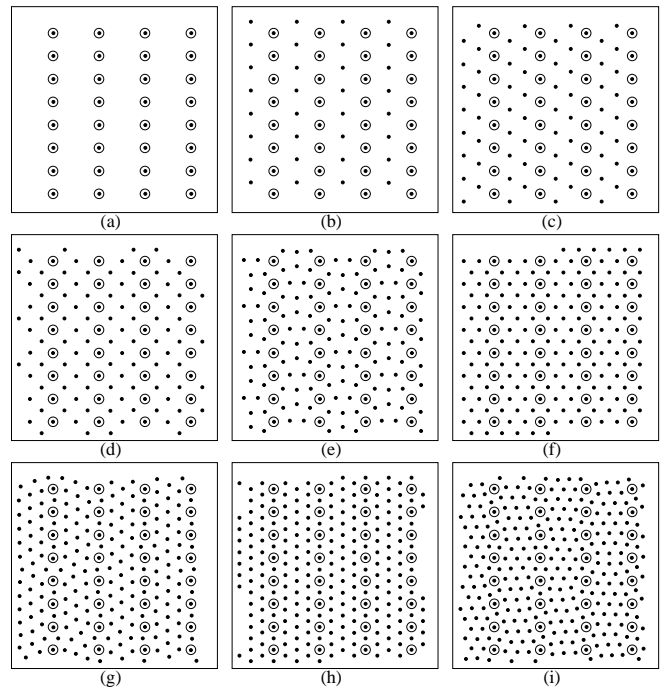


FIG. 12. Vortex positions (black circles) and pinning sites (open circles) after annealing from a higher temperature state in a rectangular pinning array with $L_x/L_y = 2$ for (a) $B/B_\phi = 1$, (b) 2, (c) 3, (d) 4, (e) 5, (f) 6, (g) 7, (h) 8, and (i) 9.

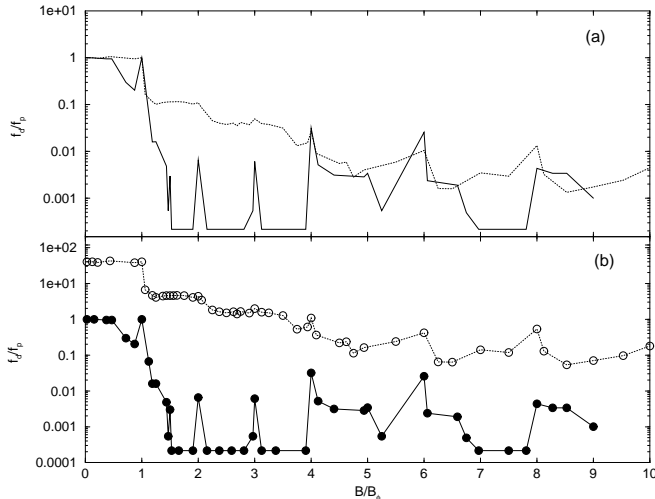


FIG. 11. Critical depinning forces versus B/B_ϕ for driving in the x and y directions for a system with a rectangular pinning array with $L_x/L_y = 2$. (a) Dashed curve is the depinning line for driving in the x -direction and the solid curve is the depinning line for driving in the y -direction. For $B/B_\phi < 4$ there is a clear anisotropy in the depinning force. The driving along the x -direction gives a higher depinning force except at $B/B_\phi = 1$, where the depinning forces both equal f_p . In (b) the same curve is plotted with the x -direction driving curve (dashed-line and open circles) shifted up for clarity. The matching peaks for the x -direction driving are strongly reduced as compared to the depinning curve for driving in the y -direction. Missing peaks for both curves occur at $B/B_\phi = 5, 7$, and 9 .

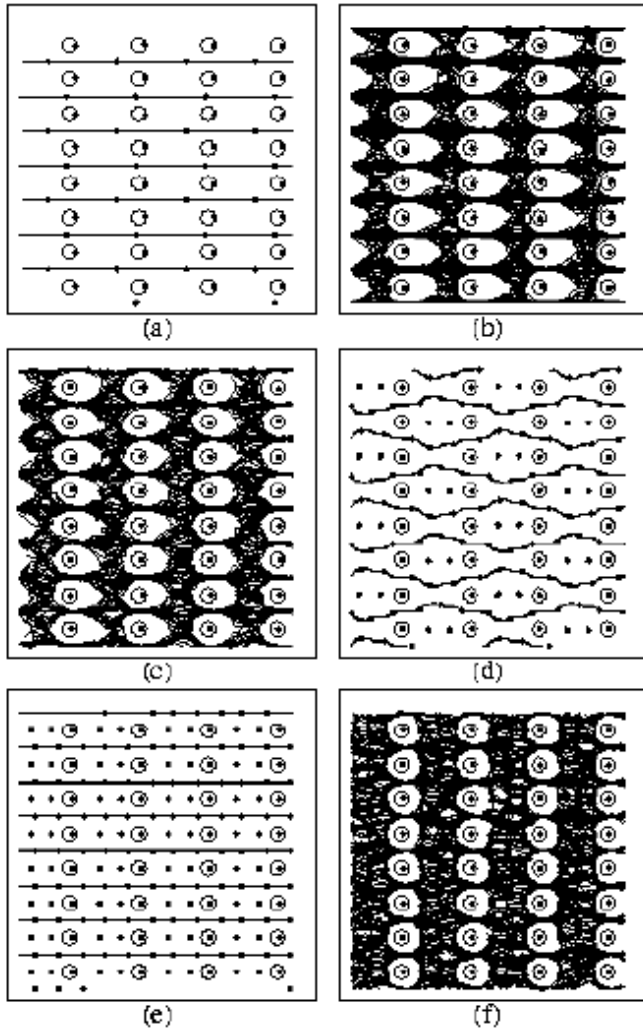


FIG. 13. Vortex trajectories for driving in the x -direction for a pinning array with $L_x/L_y = 2$. (a) $B/B_\phi = 2$, (b) 3, (c) 4, (d) 5, (e) 6, and (f) 9.

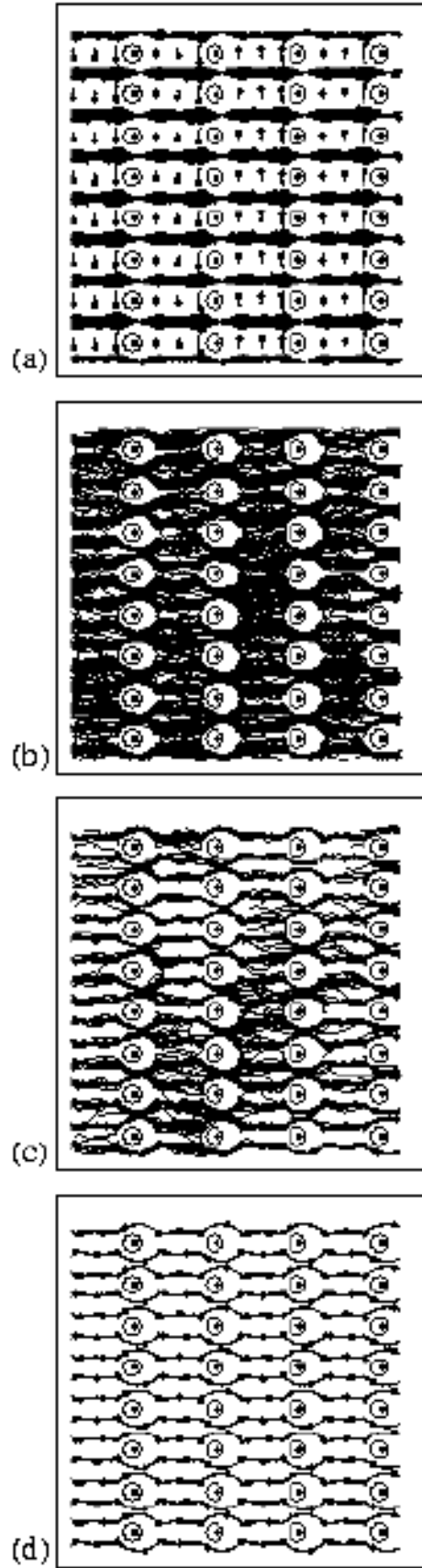


FIG. 14. Vortex trajectories for driving in the x -direction in a rectangular pinning array with $L_x/L_y = 2$ at $B/B_\phi = 8$. (a) The flow patterns for $f_d/f_p = 0.2$, where the flow is ordered and a portion of the interstitial vortices are immobile. (b) $f_d/f_p = 0.3$ flow becomes disordered. (c) $f_d/f_p = 0.35$ flow begins to reorganize. (d) $f_d/f_p = 0.37$ flow is ordered with all the interstitial vortices moving.

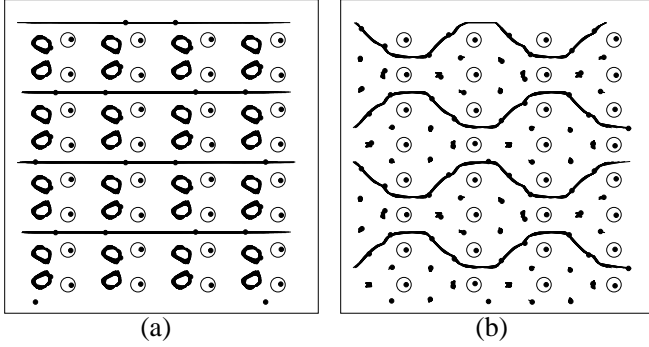


FIG. 15. Vortex trajectories for driving in the x -direction in a rectangular pinning array with $L_x/L_y = 2$ just above depinning. (a) $B/B_\phi = 2.5$; Vortex motion consists of the 1D flow of interstitial vortices between every other pinning row and the rotational motion of pairs of interstitial vortices. (b) $B/B_\phi = 4.5$; Motion consists of winding channels that weave between the pinning sites.

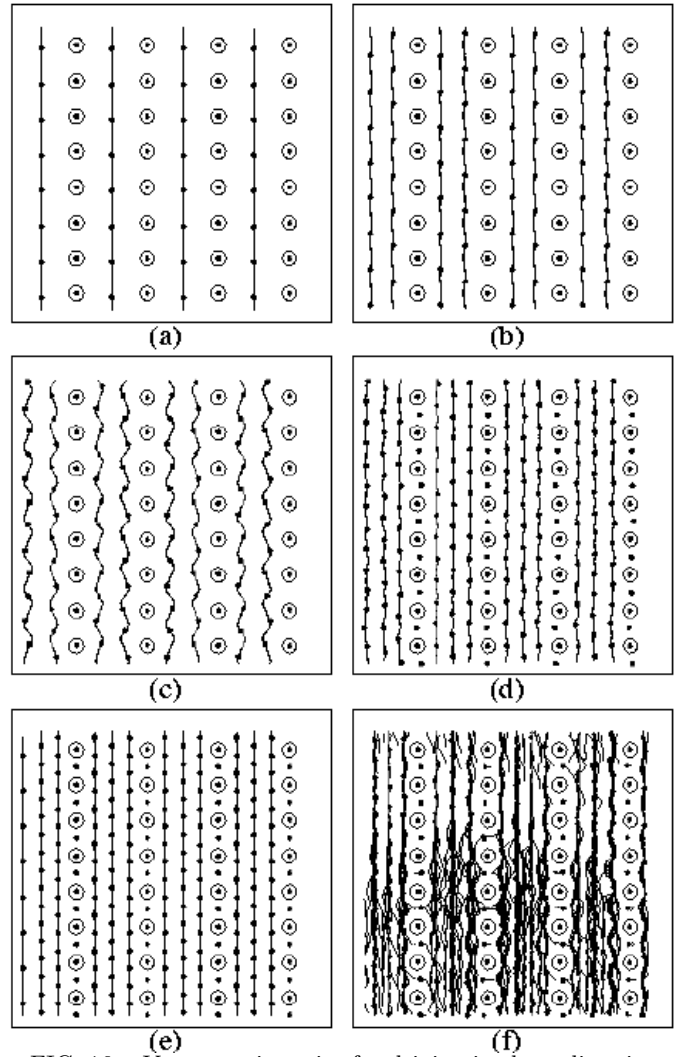


FIG. 16. Vortex trajectories for driving in the y -direction in a rectangular pinning array with $L_x/L_y = 2$, just above depinning. (a) $B/B_\phi = 2$, (b) 3, (c) 4, (d) 7, (e) 8 and (f) 9.

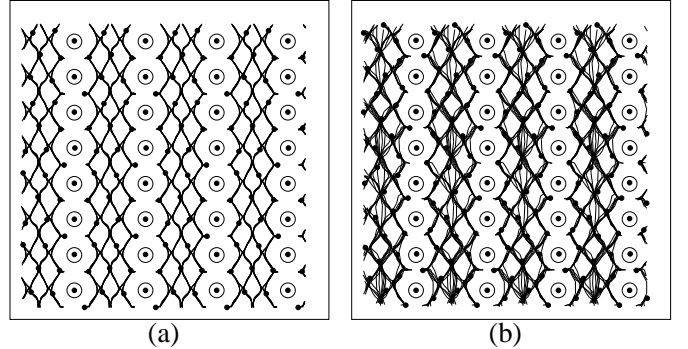


FIG. 17. Vortex trajectories for driving in the y -direction in a rectangular pinning array with $L_x/L_y = 2$, just above depinning. (a) $B/B_\phi = 5$ shows an intricate braiding flow pattern. (b) $B/B_\phi = 6$ shows a similar pattern as in (a) but with some disorder.